Open access • Journal Article • DOI:10.1109/TVT.2020.2984060

Dynamic Performance of High-Speed Railway Overhead Contact Line Interacting With Pantograph Considering Local Dropper Defect — Source link

Yang Song, Zhigang Liu, Xiaobing Lu

Institutions: Norwegian University of Science and Technology, Southwest Jiaotong University

Published on: 02 Apr 2020 - IEEE Transactions on Vehicular Technology (Institute of Electrical and Electronics Engineers (IEEE))

Topics: Contact force

Dynamic Performance of High-speed Railway Overhead Contact Line Interacting With Pantograph Considering Local Dropper Defect

Yang Song, *Member, IEEE*, Zhigang Liu, *Senior Member*, *IEEE* and Xiaobing Lu, *Member*, *IEEE*

***Abstract*—The local dropper defect is the most common fault in the early service stage of the overhead contact line (OCL) system. The plastic deformation and loose of a dropper may cause the variation of the contact line height, which has a direct effect on the contact performance of the pantograph-OCL system. This paper proposes a methodology to model the OCL with local dropper defect using a nonlinear finite element approach. Employing a developed TCUD (Target Configuration under Dead Load) method, which takes the vertical defective dropper position in the contact line as additional constraints, the local dropper defect is exactly added in the initial configuration of the OCL model. Several simulations of pantograph-OCL interaction are run with different positions of the defective dropper. The effect of local dropper defect on the pantograph-OCL contact forces is analysed. The results show that the increase of the defect degree causes the increment of the contact force peak around the defective dropper point. The defect on the first or last dropper within a span is the most detrimental to the current collection quality, as it directly causes the increase of maximum contact force, which challenges the safe operation of the pantograph-OCL system, and should be strictly restricted. The PSD (Power Spectral Density) analysis of contact force indicates that the dropper defect distorts the frequency characteristics of the contact force. The energy of contact forces decreases at the dropper-interval related frequencies due to the presence of dropper defect. Similarly, a significant 'break' of the dropper-interval frequency component can be observed in the time-frequency representation of the contact force. This phenomenon has the potential to be used to identify and locate the defective dropper from the measured contact force.**

***Index Terms*—High-speed railway, Pantograph, Overhead Contact Line, Dropper defect, Contact force, Vibration, Dynamics**

I. Introduction

In majority of electrified railways, the Overhead Contact Line (OCL) system is responsible for powering the electric train via a pantograph installed on the car body's roof. Often it is the only source of power for electric trains [1]. As shown in Figure 1, the OCL normally comprises of two tensioned cables called messenger and contact lines, which are connected by several droppers. The contact line carries the electric current to be collected by the locomotive through the sliding contact with the strip of the pantograph. The messenger line and droppers support the contact line, keeping it at the correct height which may include the reserved pre-sag. Obviously, the quality of the current collection of the electric train is directly determined by the pantograph-OCL interface. Normally, the pantograph-OCL system is the most vulnerable part in the electrified railway, as it suffers multiple impacts from the vehicle-track vibration [2], the temperature variation [3], the irregularities on the contact line [4], the unsteady wind load [5] and some other complicated disturbance [6]. The long-term service under complex work conditions leads to the degradation of the pantograph-OCL performance, which is manifested in contact line wear [7],

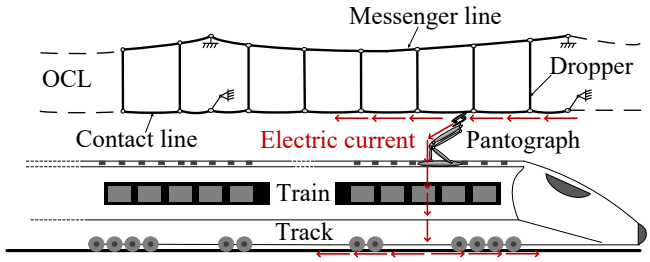

Fig. 1. Schematic of a pantograph-catenary system

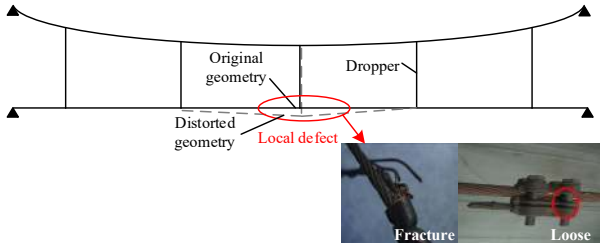

Fig. 2. Local dropper defect

This work was supported in part by the National Natural Science Foundation of China (U1734202; U51977182), and the Funding of Chengdu Guojia Electrical Engineering Co. Ltd (No. NEEC-2018-A02) (Corresponding author: Xiaobing Lu)

Yang Song is with the National Rail Transit Electrification and Automation Engineering Technique Research Center, Southwest Jiaotong University, Chengdu 611756 China. He is also with the Department of Structural Engineering, Norwegian University of Science and Technology, Trondheim, 7491 (e-mail: y.song_ac@hotmail.com).

Zhigang Liu is with the School of Electrical Engineering, Southwest Jiaotong University, Chengdu, 610031 China. (e-mail: liuzg_cd@126.com).

Xiaobing Lu is with the National Rail Transit Electrification and Automation Engineering Technique Research Center, Southwest Jiaotong University, Chengdu 611756 China. He is also with the China Railway Eryuan Engineering Group CO. LTD. (e-mail: hello.lxb@163.com).

component failure [8], and geometry distortion [9], resulting in the deterioration of the quality of current collection and the increase in the occurrence of incidents. Pantograph-OCL incidents are the major sources of traffic disruption and train delay. As is well known, the serious accidents that cause fatal consequences are generally developed from small early faults. If the early faults can be effectively coped with, the pantograph-OCL performance can be maintained in a health condition, significantly reducing the occurrence of incidents [10], and the maintenance cost .

The local dropper defect is the most common fault in the early service stage of OCL system. The long-term service, mounting errors, contact incidents, climate change and poor maintenance may result in the plastic deformation, loose and even breakage of droppers, which represent the major source of the variation of the contact line height, as illustrated in Fig. 2, and affect the vertical contact quality of the pantograph and the OCL.

In a multitude of previous studies, the pantograph-OCL simulations are usually used to verify the rationality of the design data [11], [12]. It has been demonstrated that the contact force of pantograph-OCL is the direct reflection of the contact quality. The contact force should be kept steady to ensure good contact. An inadequate contact force may increase the occurrence of arcing [13], sparking and contact loss [14], while an excessive contact force may increase the wear of the strip [15] and the contact line [16]. Normally the mean value, the standard deviation, the maximum and minimum values of contact forces are used to evaluate the contact quality of the pantograph-OCL [17]. Compared to high-cost field test, numerical tools are the more effective measures to evaluate the contact force [18]. The simulation accuracy can be guaranteed by comparison with the test data [19], laboratory test [20], standard [21] and benchmark [22]. The statistics [23], frequency components [24], and the time-frequency representations [25] of the contact force are investigated to improve the understanding of the mechanism of contact force fluctuation. The traditional view is that the uneven elasticity of the contact line is the main cause of the contact force fluctuation [26]. With the increase of the train speed, the wave propagation in the contact line plays an ever-increasing role in affecting the contact force [27]. Some effective measures, such as parameter optimization [5], [28], [29] and active control strategies [30]–[32] are proposed to ensure a good current collection quality. The effects of normal external disturbances such as the aerodynamics [33], locomotive excitation [34], wind load [35], [36] are included in the pantograph-OCL simulation to evaluate the contact forces under complex work conditions. However, most previous mathematical models of pantograph-OCL interaction do not involve the errors in the OCL system. So one of the significant development trends in this research area is to accurately model the defect in the pantograph-catenary OCL system, and evaluate its effect on the current collection quality. Most researchers focus on the detection of the OCL component faults by computer visions. The significant implication of contact line irregularities on the contact quality is firstly revealed in [37]. The OCL irregularities are mostly reproduced by ideal trigonometric functions [38]. The previous research result indicates that the variance of OCL height has a noticeable effect on the contact forces [39]. The advancement of the measurement technique facilitates the acquisition of realistic contact line heights [40], which exhibit a significant difference with respect to the design data [41]. The irregularity of the contact line presents a significant periodicity similar to the OCL structure [42], which are the main consequence of the loose and deformation of the droppers. However, the previous researches take this type of defect as the additional rigid displacement in calculating the contact force. This unrealistic assumption should be improved to include the dropper defect in the static configuration of the OCL. Pombo and Antunes [43] have acknowledged the importance to model the defective dropper in the OCL system three years ago. But the defective dropper has never been well modelled, and its effect on the contact force has never been studied in current literature. Addressing this shortcoming, this paper attempts to model the defective dropper and quantify its effect on the interaction performance of pantograph-OCL.

The research objective of this paper is the local dropper defect causing the variance of the contact line height in the early service stage of the OCL system. On the basis of a traditional FEM model of OCL, the local dropper defect is added in the shape-finding of the OCL through an advanced TCUD method. In order to understand the effect of local dropper defect on the contact forces, numerical results of the described OCL model interacted with a pantograph model, with different degrees and positions of dropper defect, are presented and analysed. Utilising the time-frequency representation of the contact forces, the potential identification method of the local dropper defect is explored. The full paper is organized by six sections. The introduction of background and the literature review are in Section I. The OCL formulations with dropper defect are described in Section II. The results of numerical simulation are presented and analysed in Section III. The identification method is discussed in Section IV. The further discussion of the results is presented in Section V. The conclusions are drawn in Section VI.

II. Modelling of OCL with dropper defect

Due to the importance of the nonlinearity of the OCL, the finite element method is the most preferred to model the OCL. In this work, a nonlinear finite element approach is adopted to model the OCL with local dropper defect. As illustrated in Fig. 3, the explicit formulas of cable are used to model the messenger/contact line and the steady arm. The nonlinear truss element is used to model the dropper. The claws on clamps of droppers and steady arms are assumed as lumped masses. Considering the local variation of the contact line height caused by the dropper defect, the configuration of the OCL is calculated by the advanced TCUD method.

A. Explicit formulas of nonlinear cable element

Considering a cable element with two nodes as shown in Fig. 3, the relative distances between the two nodes can be expressed by the nodal forces as [44]

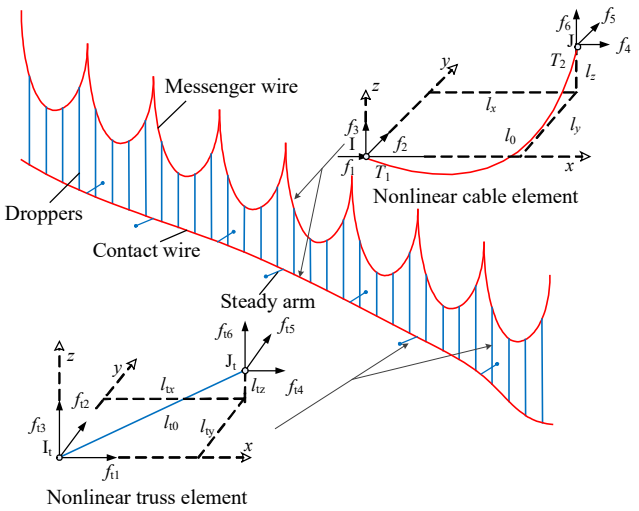

Fig. 3. OCL model with cable and truss elements

$$l_x = -(f_1 l_0)/(EA) - F_1\left\{\ln\left(\sqrt{f_4^2+f_5^2+f_6^2}+f_6\right) - \ln\left(\sqrt{f_1^2+f_2^2+f_3^2}-f_3\right)\right\}/w \tag{1a}$$

$$l_y = -f_2 l_0/(EA) + f_2\left\{\ln\left[\sqrt{f_1^2+f_2^2+(wl_0-f_3)^2} + wl_0 - f_3\right] - \ln\left(\sqrt{f_1^2+f_2^2+f_3^2}-f_3\right)\right\}/w \tag{1b}$$

$$l_z = -(f_3 l_0)/(EA) + (wl_0^2)/(2EA) + \left[\sqrt{f_4^2+f_5^2+f_6^2} - \sqrt{f_1^2+f_2^2+f_3^2}\right]/w \tag{1c}$$

where, l_x, l_y, and l_z are the relative distances along the local *x*, *y,* and *z*-axis respectively, *w* is the self-weight and l_0 is the unstrained length. *E* and *A* are Young's modulus and the cross-sectional area respectively. $f_1 \sim f_3$ and $f_4 \sim f_6$ are the nodal forces at nodes I and J, respectively. The partial differentiation of both sides of Eq. (1) yields the following incremental relationships between the relative nodal distances and nodal forces.

$$\begin{Bmatrix}\Delta l_x\\ \Delta l_y\\ \Delta l_z\end{Bmatrix} = \begin{bmatrix}\frac{\partial l_x}{\partial f_1} & \frac{\partial l_x}{\partial f_2} & \frac{\partial l_x}{\partial f_3}\\ \frac{\partial l_y}{\partial f_1} & \frac{\partial l_y}{\partial f_2} & \frac{\partial l_y}{\partial f_3}\\ \frac{\partial l_z}{\partial f_1} & \frac{\partial l_z}{\partial f_2} & \frac{\partial l_z}{\partial f_3}\end{bmatrix}\begin{Bmatrix}\Delta f_1\\ \Delta f_2\\ \Delta f_3\end{Bmatrix} + \begin{bmatrix}\frac{\partial l_x}{\partial l_0}\\ \frac{\partial l_y}{\partial l_0}\\ \frac{\partial l_z}{\partial l_0}\end{bmatrix}\Delta l_0 \tag{2}$$

Taking the inverse of the flexibility matrix in Eq. (2) yields the incremental equation of the cable element.

$$\mathbf{\Delta F}_C = \mathbf{K}_C\mathbf{\Delta U}_C + \mathbf{K}_{CL}\Delta l_0 \tag{3}$$

in which, $\mathbf{\Delta F}_C$ is the incremental nodal force vector. $\mathbf{K}_C$ is the stiffness matrix related to the nodal displacements, $\mathbf{\Delta U}_C$ is the incremental displacement vector and $\mathbf{K}_{CL}$ is the stiffness matrix related to the unstrained length of the cable.

B. Explicit formulas of nonlinear truss

The equilibrium equation of the truss element in Fig. 3 is written as follows.

$$f_{t1} = -E_t A_t\left(\frac{l_{tx}}{l_{t0}} - \frac{l_{tx}}{\sqrt{l_{tx}^2+l_{ty}^2+l_{tz}^2}}\right) \tag{4a}$$

$$f_{t2} = -E_t A_t\left(\frac{l_{ty}}{l_{t0}} - \frac{l_{ty}}{\sqrt{l_{tx}^2+l_{ty}^2+l_{tz}^2}}\right) \tag{4b}$$

$$f_{t3} = -E_t A_t\left(\frac{l_{tz}}{l_{t0}} - \frac{l_{tz}}{\sqrt{l_{tx}^2+l_{ty}^2+l_{tz}^2}}\right) \tag{4c}$$

in which $f_{t1} \sim f_{t3}$ are the nodal forces at node I_t. l_{tx}, l_{ty} and l_{tz} are the relative distances between two nodes along the local x_t, y_t and z_t axis respectively. l_{t0} is the unstrained length. E_t and A_t are Young's modulus and the cross-sectional area respectively. Considering a nonlinear dropper, $E_t A_t$ equals to zero when the dropper works in compression. Similarly, the stiffness matrix of the truss element can be obtained as:

$$\mathbf{\Delta F}_T = \mathbf{K}_T\mathbf{\Delta U}_T + \mathbf{K}_{TL}\Delta l_{t0} \tag{5}$$

in which, $\mathbf{\Delta F}_T$ is the incremental nodal force vector, $\mathbf{K}_T$ is the stiffness matrix related to the nodal displacements, and $\mathbf{\Delta U}_T$ is the incremental displacement vector. $\mathbf{K}_{TL}$ is the stiffness matrix related to the unstrained length of the truss. It should be noted that the terms related to Δl_0 and Δl_{t0} in Eqs. (3) and (5) respectively are used in the TCUD method to calculate the initial shape of the OCL. They vanish in the consequent dynamic simulations.

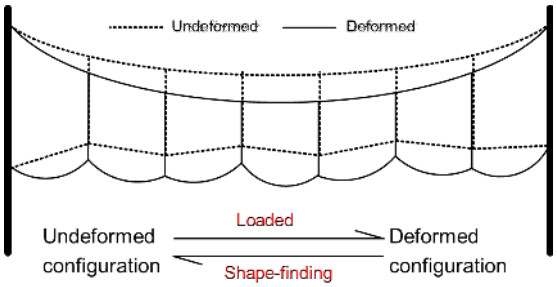

Fig. 4. Description of shape-finding of OCL

C. TCUD method

To reflect the defective dropper in the static OCL model, the shape-finding method should be employed to determine the undeformed configuration. As illustrated in Fig. 4, the deformed configuration is obtained by loading the undeformed configuration. However, in this problem, the knowns are the vertical dropper positons in the deformed configuration. The unknowns are the unstrained lengths of all the cables. In this paper, a developed TCUD method is adopted to solve this inverse problem in combination with a nonlinear finite element approach. The concept of the TCUD method is to take the unstrained length as unknown parameters, as seen in Eqs. (3) and (5), and formulate the stiffness matrix with nodal forces and unstrained length for each element [45]. In this way, more constraint conditions should be provided to eliminate the undesirable deformations of the OCL. Assembling Eqs. (3) and

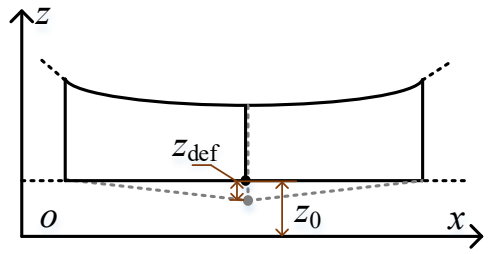

Fig. 5. Description of shape-finding of OCL

(5) by FEM, the global incremental equilibrium equation for the whole OCL can be obtained as follows.

$$\Delta\mathbf{F} = \mathbf{K}_G\Delta\mathbf{U} + \mathbf{K}_L\Delta\mathbf{L} = \begin{bmatrix}\mathbf{K}_G & \mathbf{K}_L\end{bmatrix}\begin{bmatrix}\Delta\mathbf{U}\\ \Delta\mathbf{L}\end{bmatrix} \tag{6}$$

where $\Delta\mathbf{F}$ is the unbalanced force vector. $\mathbf{K}_G$ and $\mathbf{K}_L$ are the global stiffness matrices related to the incremental nodal displacement vector $\Delta\mathbf{U}$ and the incremental unstrained length vector $\Delta\mathbf{L}$ respectively. Assume that the total number of degrees of freedom is n, and the number of elements is m. So, $\begin{bmatrix}\mathbf{K}_G & \mathbf{K}_L\end{bmatrix}$ is an $n\times(m+n)$ matrix. Since the total number of unknowns $(m+n)$ in Eq. (6) exceeds the total number of equations n, Eq. (6) has infinite solutions. Hence, additional constraint conditions should be provided to control the solution of Eq. (6), according to the design specification and the health condition. For the present case of OCL, the following additional constraint conditions are defined:

1) The vertical position of the defective dropper point in the contact line is taken as the constraint to model and control the local dropper defect. As shown in Fig. 5, the constraint condition can be defined as

$$\mathbf{U}(i_{def}) = z_0 - z_{def} \tag{7}$$

in which, i_{def} denotes the position of vertical defective dropper displacement in the vector $\mathbf{U}$. z_0 is the initial vertical position of the dropper point. z_{def} is the distortion amount caused by the defective dropper.

2) The second type of additional constraint condition is applied according to the design specification. As shown in Fig. 6, the additional constraint conditions are provided to guarantee that the deformed configuration satisfies the design requirement. Generally, there are two groups of constraints here. One is to suppress the undesired displacement:

$$\mathbf{U}(i_{design}) = z_{design} \tag{8}$$

Tab. 1. General property of OCL

Material property	
Contact wire	Line density: 1.35 kg/m; Tension: 22kN; Young's module: 1×10^{11} N/m^2; Section: 150mm^2
Messenger wire	Line density: 1.08 kg/m; Tension: 16kN; Young's module: 0.97×10^{11} N/m^2; Section: 120mm^2
Dropper	Line density: 0.117 kg/m; Tensile rigidity: 200 kN/m
Geometrical property	
Encumbrance: 1.2m; Interval of droppers: 10m; Span: 55m; Number of droppers: 5; Stagger: ±200mm; Pre-sag: 1‰	

in which, i_{design} denotes the position of all the controlled DOFs (degrees of freedom) in the vector $\mathbf{U}$. z_{design} is the designed value of all the controlled DOFs. The other constraints are the tractions applied to the endpoints of messenger and contact lines.

$$T_0 = \sqrt{f_1^2 + f_2^2 + f_3^2} \tag{9}$$

From the above additional constraint conditions, it is seen that the local dropper defect is taken as the constraint imposed on the dropper point in the contact line. These constraint conditions can supply extra m equations to reduce the numbers of unknowns in Eq. (6). So, Eq. (6) is rewritten as

$$\Delta\mathbf{F} = \mathbf{K}_G^U\Delta\mathbf{U}^U + \mathbf{K}_G^S\Delta\mathbf{U}^S + \mathbf{K}_L\Delta\mathbf{L} \tag{10}$$

where $\Delta\mathbf{U}^U$ is the unknown displacement vector to be determined by shape-finding analysis, which is an $(n\text{-}m)\times1$ vector. $\Delta\mathbf{U}^S$ is the constrained displacement vector to prevent the undesired deformation of the OCL according to the reserved pre-sag and the local defect, which is an $m\times1$ vector. $\mathbf{K}_G^U$ and $\mathbf{K}_G^S$ are the partitioned stiffness matrices corresponding to $\Delta\mathbf{U}^U$ and $\Delta\mathbf{U}^S$, respectively. Accordingly, the second term in the right-hand side of Eq. (8) vanishes, and Eq. (8) becomes

$$\Delta\mathbf{F} = \mathbf{K}_G^U\Delta\mathbf{U}^U + \mathbf{K}_L\Delta\mathbf{L} = \begin{bmatrix}\mathbf{K}_G^U & \mathbf{K}_L\end{bmatrix}\begin{bmatrix}\Delta\mathbf{U}^U\\ \Delta\mathbf{L}\end{bmatrix} \tag{11}$$

In this way, the equality between the numbers of equations and unknowns ensures the unique solution of the target configuration of the OCL. The converged nodal coordinates and unstrained lengths can be calculated iteratively by solving Eq. (11).

D. Resulting configuration with defective dropper

Without the loss of generality, the reference model in the benchmark is adopted to evaluate the effect of the defective dropper on the pantograph-catenary interaction. The general property of the OCL is presented in Tab. 1 [22]. Using the parameters of the reference model in the benchmark, an 18-span OCL model is built. Assuming that the local defect occurs on the last dropper (the ninth one) within the tenth span, the initial

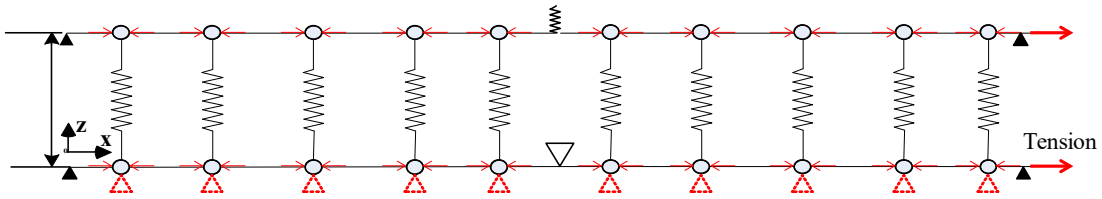

Fig. 6 Constraint conditions according to design data

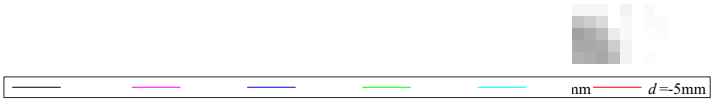

Fig. 7. Initial configuration of OCL: (a) global view; (b) side view; (c) local enlargement

Fig. 8. Configuration of contact line around defective dropper with local defect on (a) third dropper; (b) fifth dropper; (c) seventh dropper

configurations of OCL with different degrees of dropper defect are shown in Fig. 7, in which *d* denotes the vertical deviation of the defective dropper point in the contact line with respect to its original position. From Fig. 7 (a) and (b), it is seen that the local dropper defect slightly changes the initial configuration around the defective dropper. From the local enlargement in Fig. 7 (c), it is seen that the increment of the defect degree causes the increase in the deviation of the contact line height at the defective dropper point from its design position. As the defect is on the last dropper (at 545.5 m) in the tenth span, the inclination of the steady arm (at 550 m) in the adjacent span is affected slightly by the defective dropper. The two adjacent droppers (at 539.75 m and 554.5 m) before and after the defective dropper are still in their original positions. Thus, the defective dropper position can be well set by the proposed methodology without affecting others. In order to demonstrate this conclusion, the resulting configurations of contact line around the defective droppers are presented in Fig. 8 (a-c), with the local defect on the third, fifth and seventh dropper in the tenth span, respectively. It is seen that the proposed methodology can well describe the local dropper defect without affecting others.

III. Dynamic Analysis

A set of simulations are performed to explore the effect of the local dropper on the contact force. According to the benchmark, the corresponding lumped-mass model of the pantograph is built to interact with the OCL. In this section, the validation of the present model is performed against the benchmark results. Then the variation of the contact force peak caused by the local dropper defect is investigated. The frequency characteristics are also studied with the presence of dropper defect.

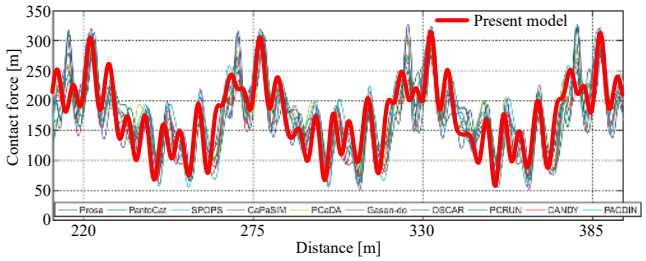

Fig. 9. Validation of contact force against benchmark

Tab. 2. Validation of geometry and elasticity against benchmark

Dropper No.	Pre-sag			Elasticity		
	Benchmark (mm)	Present (mm)	Error (%)	Benchmark (mm/N)	Present (mm/N)	Error (%)
Sup	0	0	0	0.206	0.2066	0.29
1	0	0	0	0.165	0.1698	2.91
2	24	24.00	0	0.273	0.2868	5.05
3	41	41.00	0	0.345	0.3541	2.64
4	52	52.00	0	0.388	0.4003	3.17
5	55	55.00	0	0.4	0.4085	2.12
6	52	52.00	0	0.388	0.3978	2.53
7	41	41.00	0	0.345	0.3491	1.19
8	24	24.00	0	0.273	0.2794	2.34
9	0	0	0	0.165	0.1652	0.12
Sup	0	0	0	0.206	0.2066	0.29

A. *Validation of present model*

The benchmark summarises the resulting contact forces calculated by ten participators from all over the world. The resulting contact forces are compared with the benchmark at 320km/h, as presented in Fig. 9. It is seen that both of the

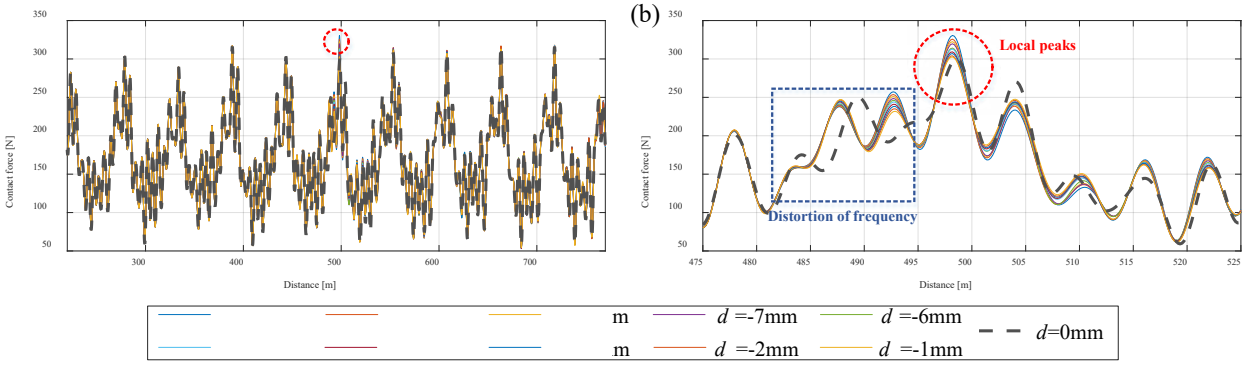

Fig. 10. Resulting contact forces with first dropper defect in tenth span: (a) global view; (b) local enlargement

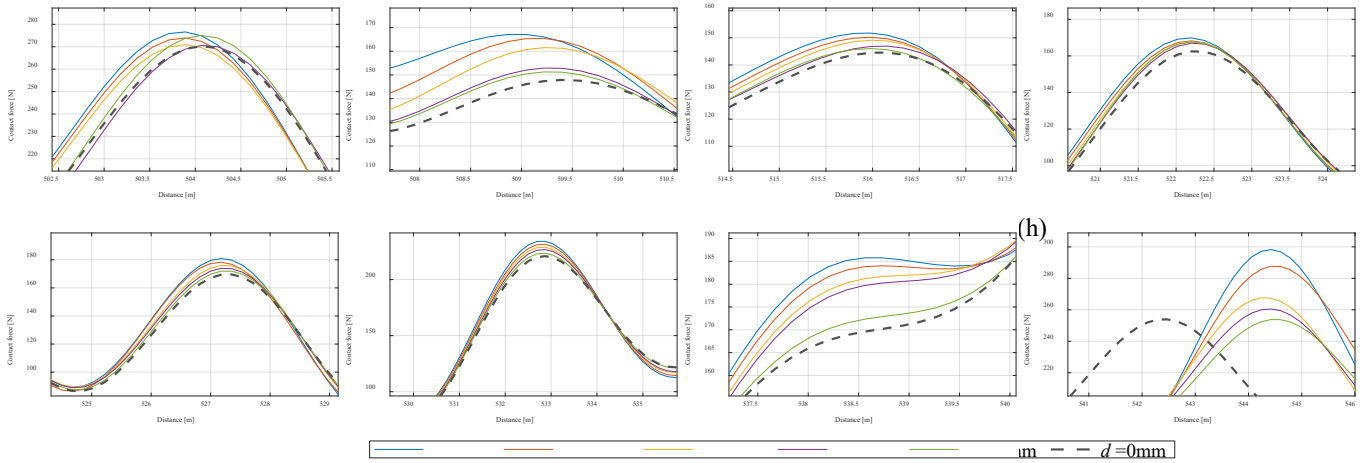

Fig. 11. Resulting contact forces around defective dropper with local defect on (a) second dropper; (b) third dropper; (c) forth dropper; (d) fifth dropper; (e) sixth dropper; (f) seventh dropper; (g) eighth dropper; (h) ninth dropper

waveform and fluctuation range of the contact forces are consistent with all the participators in the benchmark. Tab. 2 shows the validation of the elasticity and the pre-sag at the dropper and steady arm points in the contact line against the benchmark results. Due to the excellent performance of the TCUD method, the pre-sag of each dropper point is perfectly consistent with the benchmark. The largest error of the elasticity is only 5.05%, lower than the required threshold of ±10%.

B. Temporal analysis

In the simulation, the train speed is 320km/h, and the sampling frequency is 200Hz according to the benchmark. The frequency of interest is set to 0~20Hz. Normally the maximum contact force appears at the first or the last dropper point within each span, which may cause large contact line uplift and damage the OCL [46]. Considering a defect on the first dropper in the tenth span, the resulting contact forces are presented in Fig. 10 at different defect degrees. In Fig. 10 (a), it is seen that the local dropper defect cannot change the overall waveform of the contact forces. The contact force standard deviation only increases from 54.27N to 54.37 N by 0.18%, with the increase of *d* from 0 to -10mm. The most significant effect of the local dropper defect is to cause the increment of the local contact force peaks. It is seen from Fig. 7 (b) that the local maximum value increases from 300.17N to 330.61N by 10.14%, with the increase of *d* from 0 to -10mm. The excessive contact force peaks can cause additional wear of the contact surface of pantograph-OCL, and may even damage the OCL system.

It is also seen that from 480m, the contact force starts to receive the impact of the dropper defect, peaks when it is close to the defect point, and almost return to normal after 520m. The frequency of contact forces in front of the peak is distorted by the defect, which is investigated further in the following section.

Then the simulations are run with different positions of defective droppers. The resulting contact forces around each defective dropper are presented in Fig. 11. It is seen that for each defective dropper, the contact force peak appears a bit in

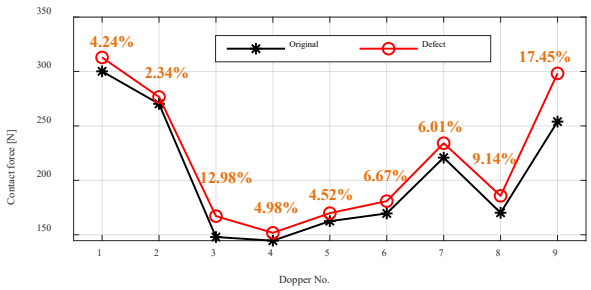

Fig. 12. Local peak of contact force around defective dropper

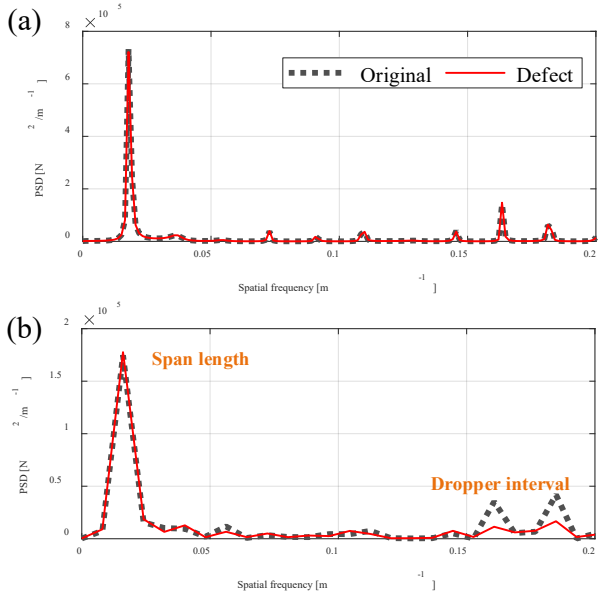

Fig. 13. PSD of contact forces with and without dropper defect: (a) global; (b) local

front of the defective dropper when the pantograph is approaching. The increase of *d* causes the significant increment of the local peak of the contact forces around the defective dropper. Some defective droppers, such as the ninth one, change the position where the local peak appears. This is also a demonstration that the dropper defect changes the frequency characteristics of the contact forces. Fig. 12 summarises the contact force peaks at around different defective droppers with d = 0 and d = -5mm. It is seen that the biggest contact force peaks appear at around the first and last dropper points. The defect on the last dropper causes the largest increase of the contact force peak. In this case, the contact force peak at around the last dropper increases from 253.94N to 298.27N by 17.45% with the increase of *d* from 0mm to -5mm. The defects on other droppers except for the first and last ones, slightly increase the local peaks of contact forces, but not affect the global maximum contact force. Therefore, more attention should be paid to the health condition of the first and last droppers within a span.

C. Frequency analysis

In order to analyse the frequency characteristics of the contact force with local dropper defect, the power spectral estimation is performed for the global contact force in Fig. 10 (a), and the local contact force in Fig. 10 (b). The corresponding PSDs are presented in Fig. 13 (a) and (b) respectively. It is seen that the PSD peaks appear at the spatial frequencies relevant to the span length and the dropper intervals. The local dropper defect cannot affect the PSD of the global contact forces. However, from the PSD of local contact forces (shown in Fig. 13 (b)) around the defective dropper, it is seen that the presence of local dropper defect makes the PSD peaks at the dropper-interval related frequency become inconspicuous. It is concluded that the local dropper defect changes the frequency characteristics of local contact forces around the defective dropper, and decreases the PSD at the dropper-interval related frequencies. This phenomenon may be utilised to identify the local dropper defect from the contact force signal. The potential of the identification method is discussed in the following section.

IV. Potential Identification Method

The frequency characteristics of local contact forces around the defective dropper have the potential to be utilised to detect and locate the defect. In this section, the time-frequency representation of contact forces is presented, and the time-frequency characteristics of contact forces with the local dropper defect are analysed.

A. Time-frequency representation

The generalized quadratic time-frequency representation $C(t,\omega;\phi)$ of the contact forces series $f(t)$ with the kernel $\phi(t,\nu)$ is defined as [47]

$$C(t,\omega;\phi)=\frac{1}{4\pi^2}\int\int\int\phi(t,\nu)e^{-j\omega\tau}e^{-j\nu(t-u)} f(u+\frac{\tau}{2})f^*(u-\frac{\tau}{2})dud\tau d\nu \tag{12}$$

where the f^* denotes complex conjugation of f . t and ω are the instantaneous time and angular frequency. u . τ and ν are the running position, time and frequency variables in the integration respectively. The quadratic time-frequency representation is obtained through a triple integral including dual Fourier transform in time $(t-u)$ and τ with the autocorrelation of contact force $f(t)$. Essentially $C(t,\omega;\phi)$ describes the signal energy distribution of contact forces in the time-frequency domain. When the kernel $\phi(t,\nu)=1$, $C(t,\omega;\phi)$ is a WVD (Wigner-Ville Distribution), which is the basic form of the quadratic class. The author's previous work [25] demonstrates that this basic form does not have good performance to describe the time-frequency characteristics of contact forces, as the WVD's variants suffer from severe interference of cross-term. In this paper, the smoothed pseudo-WVD (SPWD) is employed to reduce the interference of cross-term. The kernel of this typical quadratic time-frequency representation is expressed as follows:

$$\phi(t,\nu)=\eta(\frac{\tau}{2})\eta^*(-\frac{\tau}{2})G(\nu) \tag{13}$$

where $\eta(\tau)$ is the time window. $G(\nu)$ is a frequency window. Compared to the basic WVD kernel, the SPWD kernel acts as a filter of the WVD for the purpose to suppress the cross-term. The SPWD applies window functions independently on both the time and frequency domain of the WVD, which strongly depends on the prior information of the target signal to suppress the cross-terms correctly.

B. Identification of local defect

Employing the methodology illustrated above, the time-frequency representation of the contact forces without defective droppers is depicted in Fig. 14 (a). The resulting time-frequency representation shows high time-frequency resolution, and the most important frequency components relevant to the span

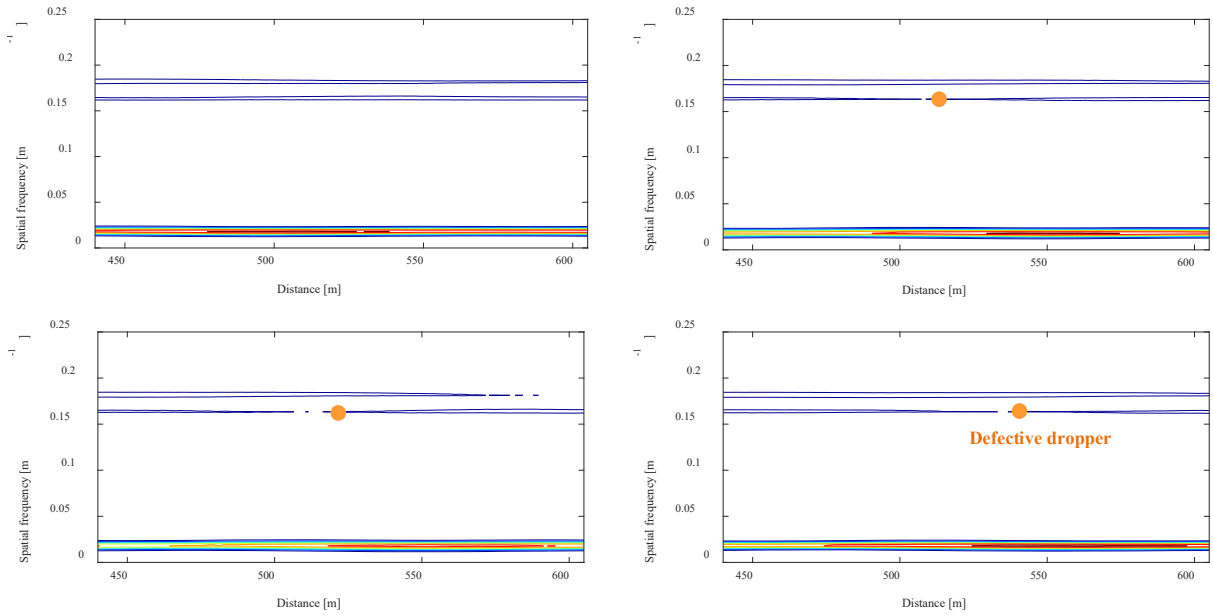

Fig. 14. Time-frequency representation of contact forces (a) without defective dropper; (b) with defect on third dropper; (c) with defect on fifth dropper; (d) with defect on ninth dropper

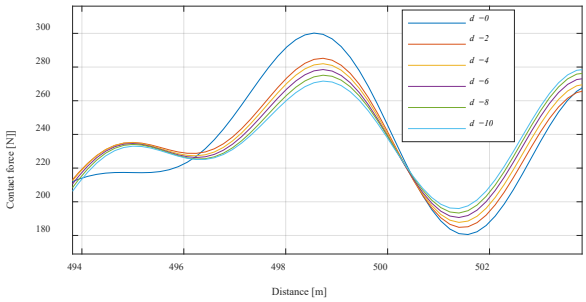

Fig. 15. Contact force around defective dropper with defect on first dropper in tenth span

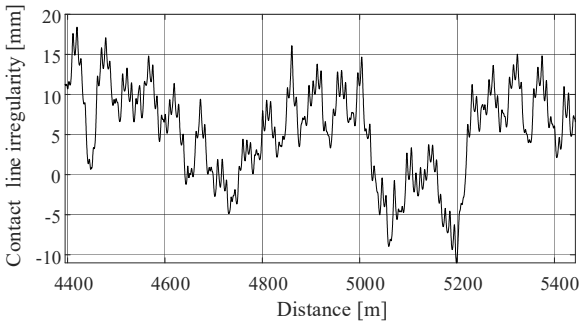

Fig. 16. Measured OCL irregularities from high-speed network

length and dropper interval can be significantly observed in the time-frequency plane. Both of these dominant frequencies are continuous along the track length. The time-frequency representation of the contact forces with the defect on the third dropper is depicted in Fig. 14 (b). The third dropper locates at the 511 m. It can be seen that a significant 'break' of the dropper-interval related frequency appears in front of the defective dropper. This phenomenon is consistent with the results of frequency analysis in Section III. The local dropper defect decreases the energy of contact forces at the dropper-interval related frequency. The similar phenomenon can also be observed from the time-frequency representations of the contact force with the defect on the fifth and ninth droppers, as presented in Fig. 14 (c) and (d), respectively. So the change of contact force frequency characteristics caused by the defective dropper can be utilized to identify and locate the defect potentially.

V. Further Discussions

The local dropper defect discussed in this paper is manifested in the excessive sag of the contact line at the defective dropper point. This type of defect is normally caused by the plastic deformation and loose of the dropper. But sometimes, reverse sag may be caused by complex work conditions e.g. temperature variation. This section discusses the effect of reverse sag of the contact line on the contact forces. Considering the defect on the first dropper in the tenth span, the contact forces around the defective dropper with reverse sags are depicted in Fig. 15. It is seen that the contact force peaks are reduced by the reverse sags. On this particular point, this type of defect can reduce the maximum contact force, and improve the safety of operation and the current collection quality. However, reverse sag may cause some other reliability issues, which deserve further detailed investigations.

The other issue is regarding the dropper defect existing in the long-term service network. This paper only models the single dropper defect and analyses its effect on the contact forces. The analysis result can improve the understanding of the variation of contact force peaks caused by the dropper defect. However, in a long-term service network, the OCL irregularities are the consequence of multiple dropper defects, which exhibit significant randomness. Fig. 16 presents realistic OCL irregularities measured from a China high-speed network. The stochastic distribution of irregularities along the track length may have a complicated effect on the dynamic performance of

pantograph-OCL interaction. The advanced stochastic analysis will be performed to evaluate the pantograph-OCL contact forces with realistic irregularities.

VI. Conclusions

The local dropper defect is the normal fault in the early service stage of OCL system. In this paper, the modelling method, the effect on contact forces, and the potential detection approach of local dropper defect are studied. The main conclusions are drawn as follows:

1) A methodology to model the railway overhead contact line with local dropper defect is developed based on the TCUD method. The local dropper defect can be exactly described in the OCL configuration.

2) The local dropper defect causes the increment of the contact force peak around the defective dropper. The most harmful defect appears at the first or last droppers within a span, which directly increases the maximum contact force. The dropper defect degree should be restricted to limit the maximum contact force.

3) The dropper defect causes the reduction of the energy at the dropper-interval related frequencies. A significant 'break' of the dropper-interval frequency component can be observed in the time-frequency representation of contact forces due to the presence of the local dropper defect. This phenomenon can be used to identify the local dropper defect through the time-frequency representation of contact forces.

Acknowledgment

This work was supported in part by the National Natural Science Foundation of China (U1734202; U51977182).

References

[1] S. Bruni, G. Bucca, M. Carnevale, A. Collina, and A. Facchinetti, "Pantograph–catenary interaction: recent achievements and future research challenges," *Int. J. Rail Transp.*, vol. 6, no. 2, pp. 57–82, 2018, doi: 10.1080/23248378.2017.1400156.

[2] D. Sinha and Omkar, "Object Drop Detection on Railway Track Through Rayleigh Wave Sensing Using Laser Vibrometer," *IEEE Trans. Veh. Technol.*, vol. 67, no. 10, pp. 9158–9172, 2018, doi: 10.1109/TVT.2018.2860578.

[3] A. Landi, L. Menconi, and L. Sani, "Hough transform and thermo-vision for monitoring pantograph-catenary system," *Proc. Inst. Mech. Eng. Part F J. Rail Rapid Transit*, vol. 220, no. 4, pp. 435–447, 2006, doi: 10.1243/0954409JRRT41.

[4] A. Collina, A. Lo Conte, and M. Carnevale, "Effect of collector deformable modes in pantograph-catenary dynamic interaction," *Proc. Inst. Mech. Eng. Part F J. Rail Rapid Transit*, vol. 223, no. 1, pp. 1–14, 2009, doi: 10.1243/09544097JRRT212.

[5] Y. Song, Z. Liu, F. Duan, X. Lu, and H. Wang, "Study on wind-induced vibration behavior of railway catenary in spatial stochastic wind field based on nonlinear finite element procedure," *J. Vib. Acoust. Trans. ASME*, vol. 140, no. 1, pp. 011010-1–14, 2018, doi: 10.1115/1.4037521.

[6] Z. Wang, Y. Song, Z. Yin, R. Wang, and W. Zhang, "Random response analysis of axle-box bearing of a high-speed train excited by crosswinds and track irregularities," *IEEE Trans. Veh. Technol.*, pp. 1–1, 2019, doi: 10.1109/tvt.2019.2943376.

[7] H. Nagasawa, T. Takahashi, Y. Horikawa, and T. Tanabe, "Development of Measuring Apparatus for Contact Wire Wear Using Sodium Vapor Lamps," *IEEJ Trans. Ind. Appl.*, vol. 116, no. 4, pp. 484–489, 1996, doi: 10.1541/ieejias.116.484.

[8] I. Aydin, M. Karaköse, and E. Akin, "A robust anomaly detection in pantograph-catenary system based on mean-shift tracking and foreground detection," *Proc. - 2013 IEEE Int. Conf. Syst. Man, Cybern. SMC 2013*, pp. 4444–4449, 2013, doi: 10.1109/SMC.2013.757.

[9] Z. Liu, W. Liu, and Z. Han, "A high-precision detection approach for catenary geometry parameters of electrical railway," *IEEE Trans. Instrum. Meas.*, vol. 66, no. 7, pp. 1798–1808, 2017, doi: 10.1109/TIM.2017.2666358.

[10] Z. Liu, Y. Song, Y. Han, H. Wang, J. Zhang, and Z. Han, "Advances of research on high-speed railway catenary," *J. Mod. Transp.*, vol. 26, no. 1, pp. 1–23, Mar. 2018, doi: 10.1007/s40534-017-0148-4.

[11] Z. Liu, S. Stichel, and A. Rønnquist, "Application of tuned-mass system on railway catenary to improve dynamic performance," *Eng. Struct.*, vol. 165, no. June 2017, pp. 349–358, 2018, doi: 10.1016/j.engstruct.2018.03.060.

[12] A. Rønnquist and P. Nåvik, "Dynamic assessment of existing soft catenary systems using modal analysis to explore higher train velocities: A case study of a Norwegian contact line system," *Veh. Syst. Dyn.*, vol. 53, no. 6, pp. 756–774, 2015, doi: 10.1080/00423114.2015.1013040.

[13] Y. Cheng, Z. Liu, and K. Huang, "Transient Analysis of Electric Arc Burning at Insulated Rail Joints in High-Speed Railway Stations Based on State-Space Modeling," *IEEE Trans. Transp. Electrif.*, vol. 3, no. 3, pp. 750–761, 2017, doi: 10.1109/TTE.2017.2713100.

[14] Z. Xu, G. Gao, Z. Yang, W. Wei, and G. Wu, "An Online Monitoring Device for Pantograph Catenary Arc Temperature Detect Based on Atomic Emission Spectroscopy," *ICHVE 2018 - 2018 IEEE Int. Conf. High Volt. Eng. Appl.*, pp. 1–4, 2019, doi: 10.1109/ICHVE.2018.8641866.

[15] P. Boffi *et al.*, "Optical fiber sensors to measure collector performance in the pantograph-catenary interaction," in *IEEE Sensors Journal*, 2009, vol. 9, no. 6, pp. 635–640, doi: 10.1109/JSEN.2009.2020244.

[16] H. Wang, A. Núñez, Z. Liu, Y. Song, F. Duan, and R. Dollevoet, "Analysis of the evolvement of contact wire wear irregularity in railway catenary based on historical data," *Veh. Syst. Dyn.*, vol. 56, no. 8, pp. 1207–1232, 2018, doi: 10.1080/00423114.2017.1408919.

[17] F. Kiessling, R. Puschmann, A. Schmieder, F. Kiebling, R. Puschmann, and A. Schmieder, *Contact Lines for Electric Railways*, Third Edit. John Wiley & Sons, 2002.

[18] Y. Song, Z. Liu, Z. Xu, and J. Zhang, "Developed moving mesh method for high-speed railway pantograph-catenary interaction based on nonlinear finite element procedure," *Int. J. Rail Transp.*, vol. 7, no. 3, pp. 173–190, 2019, doi: 10.1080/23248378.2018.1532330.

[19] D. Anastasio, A. Fasana, L. Garibaldi, and S. Marchesiello, "Analytical investigation of railway overhead contact wire dynamics and comparison with experimental results," *Mech. Syst. Signal Process.*, vol. 116, pp. 277–292, 2019, doi: 10.1016/j.ymssp.2018.06.021.

[20] B. Allotta, L. Pugi, and F. Bartolini, "Design and experimental results of an active suspension system for a high-speed pantograph," *IEEE/ASME Trans. Mechatronics*, vol. 13, no. 5, pp. 548–557, Oct. 2008, doi: 10.1109/TMECH.2008.2002145.

[21] L. Finner, G. Poetsch, B. Sarnes, and M. Kolbe, "Program for catenary-pantograph analysis, PrOSA statement of methods and validation according en 50318," *Veh. Syst. Dyn.*, vol. 53, no. 3, pp. 305–313, 2015, doi: 10.1080/00423114.2014.958501.

[22] S. Bruni *et al.*, "The results of the pantograph-catenary interaction benchmark," *Veh. Syst. Dyn.*, vol. 53, no. 3, pp. 412–435, 2015, doi: 10.1080/00423114.2014.953183.

[23] J. Pombo and J. Ambrosio, "Environmental and track perturbations on multiple pantograph interaction with catenaries in high-speed trains," *Comput. Struct.*, vol. 124, pp. 88–101, 2013, doi: 10.1016/j.compstruc.2013.01.015.

[24] J. Zhang, W. Liu, and Z. Zhang, "Study on Characteristics Location of Pantograph-Catenary Contact Force Signal Based on Wavelet Transform," *IEEE Trans. Instrum. Meas.*, vol. 68, no. 2, pp. 402–411, 2019, doi: 10.1109/TIM.2018.2851422.

[25] H. Wang *et al.*, "Detection of Contact Wire Irregularities Using a Quadratic Time-Frequency Representation of the Pantograph-Catenary Contact Force," *IEEE Trans. Instrum. Meas.*, vol. 65, no. 6, pp. 1385–1397, 2016, doi: 10.1109/TIM.2016.2518879.

[26] T. X. Wu and M. J. Brennan, "Dynamic stiffness of a railway overhead wire system and its effect on pantograph-catenary system dynamics," *J. Sound Vib.*, vol. 219, no. 3, pp. 483–502, 1999, doi: 10.1006/jsvi.1998.1869.

[27] Y. Song, Z. Liu, F. Duan, Z. Xu, and X. Lu, "Wave propagation

analysis in high-speed railway catenary system subjected to a moving pantograph," *Appl. Math. Model.*, vol. 59, pp. 20–38, 2018, doi: 10.1016/j.apm.2018.01.001.

[28] Z. Qu, S. Yuan, R. Chi, L. Chang, and L. Zhao, "Genetic optimization method of pantograph and catenary comprehensive monitor status prediction model based on adadelta deep neural network," *IEEE Access*, vol. 7, pp. 23210–23221, 2019, doi: 10.1109/ACCESS.2019.2899074.

[29] S. Gregori, M. Tur, E. Nadal, and F. J. Fuenmayor, "An approach to geometric optimisation of railway catenaries," *Veh. Syst. Dyn.*, vol. 56, no. 8, pp. 1162–1186, 2018, doi: 10.1080/00423114.2017.1407434.

[30] Y. Song, Z. Liu, H. Ouyang, H. Wang, and X. Lu, "Sliding mode control with PD sliding surface for high-speed railway pantograph-catenary contact force under strong stochastic wind field," *Shock Vib.*, vol. 2017, pp. 4895321-1–16, Jan. 2017, doi: 10.1155/2017/4895321.

[31] Y. C. Lin, C. L. Lin, and C. C. Yang, "Robust active vibration control for rail vehicle pantograph," *IEEE Trans. Veh. Technol.*, vol. 56, no. 4 II, pp. 1994–2004, 2007, doi: 10.1109/TVT.2007.897246.

[32] Y. Song, H. Ouyang, Z. Liu, G. Mei, H. Wang, and X. Lu, "Active control of contact force for high-speed railway pantograph-catenary based on multi-body pantograph model," *Mech. Mach. Theory*, vol. 115, pp. 35–59, 2017, doi: 10.1016/j.mechmachtheory.2017.04.014.

[33] M. Carnevale, A. Facchinetti, and D. Rocchi, "Procedure to assess the role of railway pantograph components in generating the aerodynamic uplift," *J. Wind Eng. Ind. Aerodyn.*, vol. 160, no. July 2016, pp. 16–29, 2017, doi: 10.1016/j.jweia.2016.11.003.

[34] A. Carnicero, J. R. Jimenez-Octavio, C. Sanchez-Rebollo, A. Ramos, and M. Such, "Influence of track irregularities in the catenary-pantograph dynamic interaction," *J. Comput. Nonlinear Dyn.*, vol. 7, no. 4, p. 041015, Jul. 2012, doi: 10.1115/1.4006735.

[35] Y. Song, Z. Liu, H. Wang, J. Zhang, X. Lu, and F. Duan, "Analysis of the galloping behaviour of an electrified railway overhead contact line using the non-linear finite element method," *Proc. Inst. Mech. Eng. Part F J. Rail Rapid Transit*, vol. 232, no. 10, pp. 2339–2352, 2018, doi: 10.1177/0954409718769751.

[36] Y. Song, Z. Liu, H. Wang, X. Lu, and J. Zhang, "Nonlinear analysis of wind-induced vibration of high-speed railway catenary and its influence on pantograph–catenary interaction," *Veh. Syst. Dyn.*, vol. 54, no. 6, pp. 723–747, 2016, doi: 10.1080/00423114.2016.1156134.

[37] W. Zhang, G. Mei, and J. Zeng, "A study of pantograph/catenary system dynamics with influence of presag and irregularity of contact wire," *Veh. Syst. Dyn.*, vol. 37, no. SUPPL., pp. 593–604, 2003, doi: 10.1080/00423114.2002.11666265.

[38] J. P. Massat, E. Balmes, J. P. Bianchi, and G. Van Kalsbeek, "OSCAR statement of methods," *Veh. Syst. Dyn.*, vol. 53, no. 3, pp. 370–379, 2015, doi: 10.1080/00423114.2015.1005016.

[39] O. V. Van, J. P. Massat, C. Laurent, and E. Balmes, "Introduction of variability into pantograph-catenary dynamic simulations," *Veh. Syst. Dyn.*, vol. 52, no. 10, pp. 1254–1269, 2014, doi: 10.1080/00423114.2014.922199.

[40] A. Collina, F. Fossati, M. Papi, and F. Resta, "Impact of overhead line irregularity on current collection and diagnostics based on the measurement of pantograph dynamics," *Proc. Inst. Mech. Eng. Part F J. Rail Rapid Transit*, vol. 221, no. 4, pp. 547–559, 2007, doi: 10.1243/09544097F02105.

[41] P. Nåvik, A. Rønnquist, and S. Stichel, "Variation in predicting pantograph–catenary interaction contact forces, numerical simulations and field measurements," *Veh. Syst. Dyn.*, vol. 55, no. 9, pp. 1265–1282, 2017, doi: 10.1080/00423114.2017.1308523.

[42] H. Wang, Z. Liu, A. Núñez, and R. Dollevoet, "Entropy-Based Local Irregularity Detection for High-Speed Railway Catenaries with Frequent Inspections," *IEEE Trans. Instrum. Meas.*, vol. 68, no. 10, pp. 3536–3547, 2019, doi: 10.1109/TIM.2018.2881529.

[43] P. Antunes, J. Ambrósio, and J. Pombo, "Catenary finite element model initialization using optimization," in *Civil-Comp Proceedings*, 2016, vol. 110, doi: 10.4203/ccp.110.106.

[44] Y. Song, Z. Liu, H. Wang, X. Lu, and J. Zhang, "Nonlinear modelling of high-speed catenary based on analytical expressions of cable and truss elements," *Veh. Syst. Dyn.*, vol. 53, no. 10, pp. 1455–1479, 2015, doi: 10.1080/00423114.2015.1051548.

[45] H. K. Kim and M. Y. Kim, "Efficient combination of a TCUD method and an initial force method for determining initial shapes of cable-supported bridges," *Int. J. Steel Struct.*, vol. 12, no. 2, pp. 157–174, 2012, doi: 10.1007/s13296-012-2002-1.

[46] *EN 50367. Railway applications — Current collection systems — Technical criteria for the interaction between pantograph and overhead line.*, no. August 2013. 2016.

[47] L. Cohen, "Generalized phase-space distribution functions," *J. Math. Phys.*, vol. 7, no. 5, pp. 781–786, 1966, doi: 10.1063/1.1931206.

Yang Song (S'16–M'19) received the Ph.D. degree in electrical engineering from Southwest Jiaotong University, Sichuan China, in 2018. He worked as a Research Fellow with the Institute of Railway Research, School of Computing and Engineering, University of Huddersfield, UK from 10/2018 to 09/2019. He is currently a Postdoctoral Fellow at Department of Structural Engineering, Norwegian University of Technology, Norway. His research interests involve the assessment of railway pantograph-catenary interaction, the wind-induced vibration of long-span structures of railway transportation, and the coupling dynamics in railway engineering.

Zhigang Liu (M'06–SM'16) received the Ph.D. degree in power system and its automation from the Southwest Jiaotong University, Sichuan, China, in 2003.

He is currently a Full Professor with the School of Electrical Engineering, Southwest Jiaotong University, China. His current research interests include the electrical relationship of vehicle-grid in high-speed railway, pantograph-catenary interaction, and status assessment.

Prof. Liu was awarded the fellowship of the Institute of Engineering and Technology in 2017. He is an Associate Editor of the IEEE Transactions on Instrumentation and Measurement, IEEE Transactions on Vehicular Technology and IEEE Access.

Xiaobing Lu (S'16–M'19) received the Ph.D. degree in electrical engineering from Southwest Jiaotong University, Sichuan China, in 2018. He is currently an engineer at the China Railway Eryuan Engineering Group CO. LTD.

His current research interests include the pantograph-catenary system modelling and the active control of pantograph.